Surface & Coatings Technology 507 (2025) 132147

Contents lists available at ScienceDirect

Surface & Coatings Technology

journal homepage: www.elsevier.com/locate/surfcoat

Microstructure evolution and water vapor resistance of multi-layer EB-PVD yttrium-based EBCs

Cynthia Y. Guijosa-Garcia *, Klemens Kelm, Uwe Schulz, Ravisankar Naraparaju

Institute of Materials Research, German Aerospace Center (DLR), 51147 Cologne, Germany

ARTICLE INFO

Keywords:
EBC
EB-PVD
Double layer
YMS/YDS
Water vapor
Oxidation

ABSTRACT

Electron beam physical vapor deposition (EB-PVD) is a promising deposition technique to produce environmental barrier coatings (EBCs) to protect ceramic matrix composites (CMCs) for complex components in aircraft engines with sharp edges such as vanes or blades. The main focus of this study was establishing an initial parameter set for depositing a multi-layer yttrium mono−/di-silicate (YMS/YDS) EBCs using EB-PVD. YMS and YDS layers show a dense microstructure without feather-arms and opened inter-columnar gaps in the as deposited state. EB-PVD EBCs were found to be amorphous in the as-coated condition, and a crystallization heat treatment was needed. Oxidation tests of EBCs were also carried out under "air condition" (1400 °C, 100 h, 100 wt% air) and "wet condition" (1300 and 1400 °C, 100 h, 30 wt% H_2O/70 wt% air) to get the preliminary assessment of the degradation. The YMS top layer has undergone slight morphological changes such as porosity and crack network formation. The YMS layer has exhibited a phase separation into Y_2O_3 and X2-YMS after the oxidation. No noticeable degradation of YDS due to water vapor oxidation was found. However, few polymorphs were observed in the YDS layer along with few cracks during various stages of the heat treatments.

1. Introduction

Ceramic matrix composites (SiC/SiC-CMCs) have been commercially implemented in the hot section of gas turbine engines to enhance temperature capability, strength-to-weight ratio, and to contribute to CO_2 reduction. CMCs have been used as components for static parts, e.g., combustors, shrouds, and nozzles, characterized by slightly curved geometry [1,2]. Currently, CMCs are being considered for application to components like vanes with a complex geometry that includes sharp edges.

SiC-SiC_f based components are exposed to the hot gas flow containing considerable amounts of water vapor, which will accelerate the recession of the protective SiO_2 scale through the formation of gaseous species ($Si(OH)_x$), limiting the lifetime of the components [3,4]. Therefore, environmental barrier coatings (EBCs) have been applied on the surface to mitigate the adverse effect of water vapor. The state-of-the-art EBC system comprises of two or more layers, namely bond coat for oxidation protection and a second layer against water vapor diffusion known as top coat [5,6]. The EBC architecture was designed to be impervious (dense and crack-free) and have a matching coefficient of thermal expansion similar to solid CMCs [7]. Dense EBCs reduce the possibility of oxygen and steam transport to the SiC-based component.

Atmospheric plasma spray (APS) is currently considered as the standard method to produce EBCs with a porosity of ~4–7 % on semi-angular geometries such as static components [5,8]. Rare earth disilicates, $RE_2Si_2O_7$, (REDS), are applied as standard EBC materials. However, plasma spraying induces silica loss and causes the formation of additional phases like monosilicate, RE_2SiO_5 (REMS) [9]. Manufacturing EBCs by APS on sharp geometries is still a challenging task. Physical vapor deposition (PVD) methods, such as reactive magnetron sputtering, have been successfully applied to produce EBCs based on YMS/YDS and YbMS/YbDS on complex geometries. Reactive magnetron sputtering produces nearly stoichiometric, well-adherent EBCs onto the Si-bond coat, even on curved surfaces [10,11]. Nevertheless, the reactive sputtering method is limited in terms of attaining a larger coating thickness then approx. 20 μm in an economic way. The Electron-beam physical vapor deposition (EB-PVD) technique has already been used to coat thick thermal barrier coatings (TBCs) on turbine blades [12]. The higher deposition rate of the EB-PVD method offers a potential deposition solution to coat curved or sharp objects, such as blades, vanes, etc., with thicker and dense EBCs. Generally, the EB-PVD coatings are characterized by a columnar microstructure with

* Corresponding author.
E-mail address: cynthia.garcia@dlr.de (C.Y. Guijosa-Garcia).

https://doi.org/10.1016/j.surfcoat.2025.132147
Received 20 January 2025; Received in revised form 17 March 2025; Accepted 7 April 2025
Available online 8 April 2025

inter columnar porosity, zirconia- and alumina-based coatings [13–15]. The EB-PVD process offers wide range, great possibilities for controlling the microstructure and composition of various materials [14,16,17]. The development of EBCs using EB-PVD is taking its initial steps. Zun and Hurst, developed a EBC system on CMC specimen, consisted of a thin bond coat (HfO_2-Si) layer and follow by a top coat layer EBC (Yb, Gd)$_2Si_2O_7$ [18]. Tokoi et al. reported the deposition of $Yb_2Si_2O_7$ using two sources SiO_2 and Yb_2O_3, resulted in a dense, crack-free, and thicker coating (~30 μm) using an additional substrate heater during the deposition time [19]. In principle, RE-silicates can be deposited by EB-PVD either from one or two metallic ingots by reactive deposition and addition of oxygen in the vapor phase, or by evaporation of oxide ingots. Since the vapor pressures of yttria and silica differ considerably, evaporation from one molten pool containing both oxides will not properly work and the resulting coating will show fluctuation in chemistry. Therefore, two-source evaporation is the preferred way to produce EB-PVD EBCs.

Ytterbium disilicate (YbDS) is the widely used material for EBCs due to its high temperature phase stability ~1600 °C and its favorable CTE [9,8,11]. Yttrium mono- and di-silicate are also attractive for EBC applications [10,20]. YMS presents lower thermal conductivity and better CMAS resistance than YbDS [21,22]. YDS undergoes four polymorphic phases until its melting point associated with volume changes (α, β, γ, and δ) become not suitable for EBC applications [23]. On the other hand, YDS usually has a lower CTE than YMS, which fits better to the one of the CMC. Combining of both YMS (top layer) and YDS (β or γ, intermediate layer) as a double layer on top of SiC would minimize the thermal stress caused by CTE mismatch and can also reduce the thermal conductivity. Simultaneously, double layer system can offer better CMAS and water vapor resistance through the YMS top layer. In addition, yttrium silicates represent economic advantages. This study aims to evaluate the possibilities of evaporation of two oxide ingots to deposit a double-layer YMS/YDS system on a SiC substrate using the EB-PVD process, and to establish a starting set of suitable processing conditions. The thermochemical stability and microstructure evolution of the coatings under dry and wet oxidation conditions at 1300 °C, and 1400 °C is studied in detail.

2. Experimental methods

2.1. Coating production

An EBC multilayer coating was produced using the EB-PVD technique (ESPRI, von Ardenne GmbH, Dresden, Germany). YDS and YMS layers were coated on monolithic α-SiC substrates with dimensions of ø30 × 3 mm without Si-bond coat, (Hexoloy SA, CoorsTek GmbH, Mönchengladbach, Germany). In addition, an Al_2O_3 substrate was coated in the same run that had a lower surface roughness and a higher degree of flatness, which is favorable to study the initial coating microstructure and lowering the influence of surface roughness on the growth and microstructure of the coating. YMS and YDS coatings were produced using a jumping beam system by co-evaporation from two sources, namely Y_2O_3 and SiO_2. The samples were mounted on a mandrel and rotated during the co-evaporation as described in Fig. 1. The rotation speed was fixed at 15 rpm while the evaporation time of 12 min at a deposition rate of ~2.8 and 3.19 μm/min were set to get the desired thicknesses for YMS and YDS layers, respectively. The electron beam power, beam patterns, dwell times on each ingot and jumping frequencies were established in a number of pre-trials to get a fairly homogeneous and relatively stable evaporation from both pools. By setting those conditions, two vapor clouds from Y_2O_3 and SiO_2 ingots were produced. The samples were mounted between the Y_2O_3 and SiO_2 clouds, as shown in Fig. 1. The YMS composition was found in the vapor cloud which lies closer to the Y_2O_3 ingot whereas the YDS chemistry was found at an intermediate distance between the two ingots. The exact position for YMS and YDS composition was determined based on several initial coating runs. For the final EBC system, the YDS layer was deposited first and moved out of the coating chamber and then cooled down to RT. In a second run, the samples were moved after pre-heating into the coating chamber to the YMS position and to get the second layer. The EBC design for this preliminary work did not include a Si bond coat as a base layer. Therefore, the coating architecture consists of SiC + YDS + YMS. As deposited, YDS/YMS coatings were found to be amorphous, and an additional crystallization treatment was carried out at 1250 °C, 2 h, under laboratory air conditions.

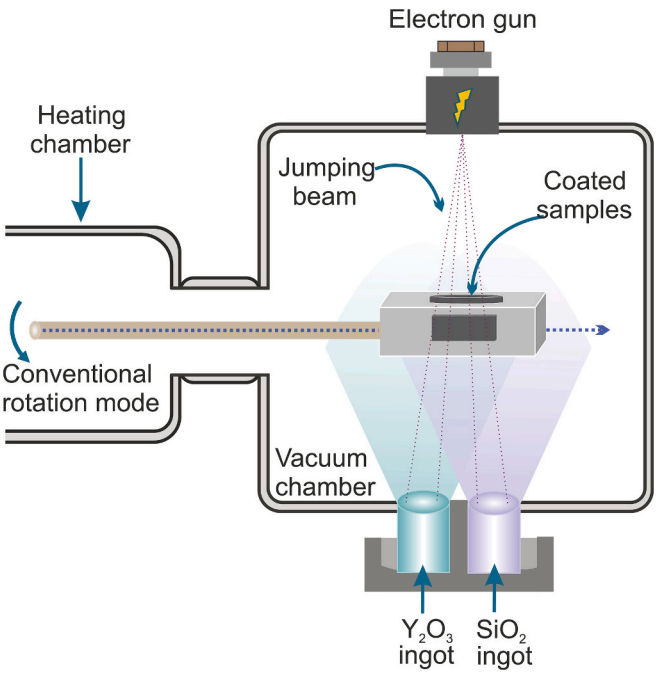

Fig. 1. Diagram of a typical electron beam evaporation process of two sources.

2.2. Air and steam oxidation test

Four equi-sized specimens were cut from the EBC sample after the crystallization treatment to evaluate the final microstructure and perform different oxidation tests on the identical coatings. The cutting process might have induced stresses and led to an internal crack formation within the coating on those quite small specimens. The following oxidation tests were carried out in a preheated tube furnace (alumina tube (ø70 × 1200 mm), Carbolite Gero GmbH, HTRH 17/70/300, Germany):

a) Isothermal oxidation for 100 h at 1400 °C in lab air conditions using a tube furnace (named here as "air condition").
b) Isothermal oxidation for 100 h at 1300 and 1400 °C in 30 wt% H_2O/70 wt% lab air (named here as "wet condition").

Under wet condition, a flow rate of 0.02 l/h was maintained throughout all experiment. The use of this quasi-static flow is not expected to cause significant recession from silica loss; however, different reactions between air and wet conditions in the EBCs are anticipated. Moreover, these conditions were selected to understand the corresponding effects, such as sintering and phase changes in EB-PVD EBC microstructure. The specimens were quickly removed out of the tube after 100 h and quenched to room temperature while maintaining the wet conditions. The associated thermal shock has initiated spallation of the coating, which allowed us to study the ~80 μm thick free-standing EBCs. However, only partial spallation was observed for oxidation under air conditions.

2.3. Characterization

EBC phase analysis was carried out by X-ray diffraction (XRD) using a CuK_α ($\lambda = 1.5406$ Å) cathode operating at 35 kV and 30 mA (D8 Discovery with a Lynxeye XE-detector, Bruker AXS, Karlsruhe, Germany). The measuring 2θ-range was set between 10 and 90°, with a step size of 0.02° and 2°/min scan rate. The Rietveld method was employed to quantify the phase constituents. All the specimens were mounted in epoxy resin following a standard metallographic technique to prepare the cross-sections for scanning electron microscopy (SEM, Ultra 55, Carl Zeiss NTS, Oberkochen, Germany) equipped with an energy dispersive X-ray spectroscopy system (EDS, Aztec, Oxford Instruments, Abingdon, UK). Suitable lamellae for transmission electron microscopy (TEM) were extracted from regions of interest using dual beam/focused ion beam system (FIB, Dual Beam FEI Helios 600i, FEI, Hillsboro, Or, USA). Transmission electron microscopy (TEM) experiments were conducted at 300 keV beam energy both in scanning (STEM) and static beam mode (Tecnai F30, Philips Electron Optics, Eindhoven, The Netherlands). The microscope is equipped with a conventional bright field−/dark field detector (Philips) and a bottom mounted CCD-camara (Gatan Model 794, Gatan, Warrendale, PA, USA). A high angle annular dark field (HAADF) detector (Fischione, Export, PA, USA) was used for *Z*-contrast imaging in conjunction with EDS (Apollo XLTW, EDAX, Mahwah, NJ, USA).

3. Results

3.1. Microstructure of the as coated EBC layers

Fig. 2 illustrates the surface and cross-section morphologies of as-coated YMS/YDS EBCs on alumina substrate. The coatings were well-adherent to the alumina substrate. The top-view microstructure consists of typical EB-PVD columns (~2–5 μm diameter) exhibiting very thin columnar gaps (Fig. 2a). Microstructural defects such as spitting (bubble-like morphologies) and few cracks were also observed (Fig. 2b). The YMS/YDS cross-sectional morphology exhibits a rather dense, more vitreous microstructure with a sharp, intact YDS/YMS interface (Fig. 2c). Both layers reveal a nano-layer formation that corresponds to each rotation of the sample during deposition through the SiO_2 and Y_2O_3 clouds (Fig. 2d,e). Each nano-layer was heavily enriched in either yttrium or silicon in alternating arrangement. Spitting deposition defects are seen as a conical gap through the cross-section (Fig. 2c). The thicknesses of YMS and YDS layers were measured as 34 μm and 38 μm, respectively. The Y:Si average ratio measured by EDS for the YMS and YDS layers are 2.8 (±0.19) and 0.75 (±0.1), respectively. Based on the theoretical ratio for $Y_2SiO_5 = 2$ and $Y_2Si_2O_7 = 1$, it can be stated that YMS coating was enriched with yttrium and the YDS layer with Si. The yttrium silicate layers were nearly oxygen saturated. An additional post deposition oxidation was not required. No reaction was observed either with the Al_2O_3 (Fig. 2e) or with the SiC substrate (not shown) after deposition.

3.2. Crystallization of YMS and YDS layers

XRD patterns of crystallized YMS and YDS after the heat treatment are presented in Fig. 3. The YMS layer was measured on the coating attached to the SiC, while the YDS layer was assessed on a small piece of the coating that was mechanically detached from the substrate using forceps. Due to the smaller size of the pulled chunk of YDS, the diffractogram is somewhat noisy and not suitable for further more sophisticate analysis e.g. Rietveld refined. The XRD patterns of YMS at 1250 °C exhibited primarily the X2-YMS (*I2/a*, space group) phase and minor peaks of the Y_2O_3 phase (I*a3*, space group) (Fig. 3a). The phase percentages were calculated using the Rietveld method, resulting in 93 % for YMS and a low fraction of 7 % for Y_2O_3. On the other hand, the α-YDS (*P-1*, space group) and β-YDS (*C2/m*, space group) polymorphs were identified in the YDS layer (Fig. 3b). The peaks around 22° and 34° are attributed to SiO_2 (likely formed during the crystallization treatment) and SiC, which is assumed to originate from the EBC/SiC interface due to the mechanical removal of the coating.

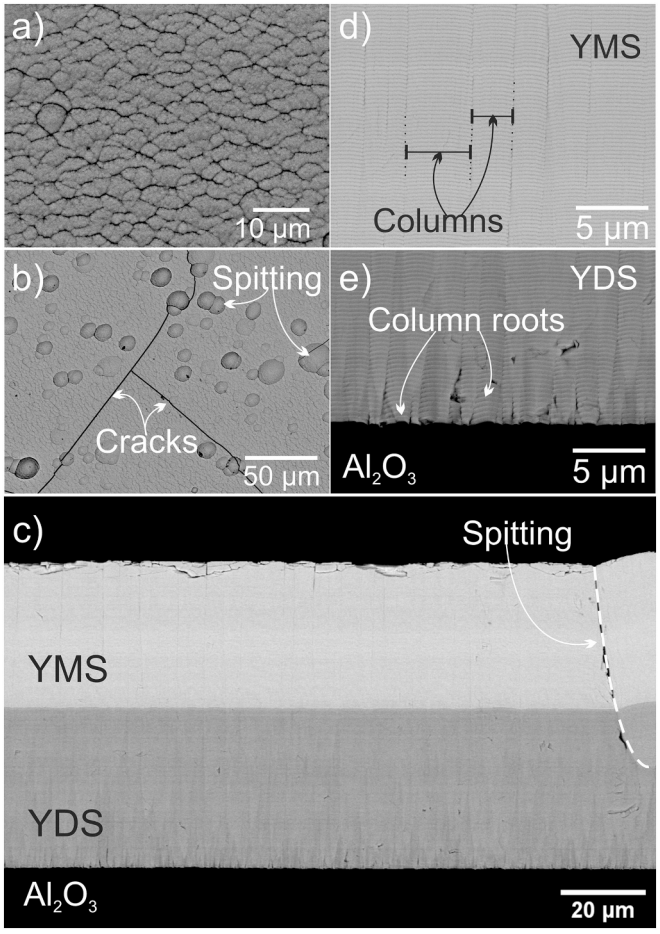

Fig. 2. BSE micrographs of as-coated multi-layer YMS/YDS EBC on Al_2O_3 substrate: top view in high (a) and low (b) magnification, c) cross-section of both layers, d) high magnification of YMS layer, and e) YDS layer.

After the crystallization heat treatment, the YMS surface has undergone few morphological changes such as densification of grains, crack formation along spitting defects (Fig. 4b). The initial columns are no longer visible in top view. Instead, larger round or elongated grains have formed. Although the surface exhibits a more pronounced network of cracks due to the crystallization treatment, the cross-section still appears dense (Fig. 4a). After the crystallization heat treatment, the thickness of each layer increases by 1 and 4.4 μm for YMS and YDS, respectively (Table 1). The thickness was measured using a SEM image and compared with the as-deposited coating thickness. An important observation in the case of YMS microstructure is the presence of an array of alternative nano-layers of YMS (dark layers) and Y_2O_3 (bright layers), as shown in Fig. 4c. Meanwhile, the YDS coating shows a more homogeneous arrangement of single-phase nano-layers exhibiting even a visible formation of rounded grains (Fig. 4d). EDS spot analysis results (not shown) confirmed the chemical composition of YMS, Y_2O_3, and YDS on corresponding layers. The EBC exhibited and excellent adhesion with the SiC after crystallization, and no spallation was observed. Overall, a dense microstructure was still presumed after the heat treatment.

3.3. Isothermal oxidation under air condition

Fig. 5a and b show the top view and cross-section of the resulting

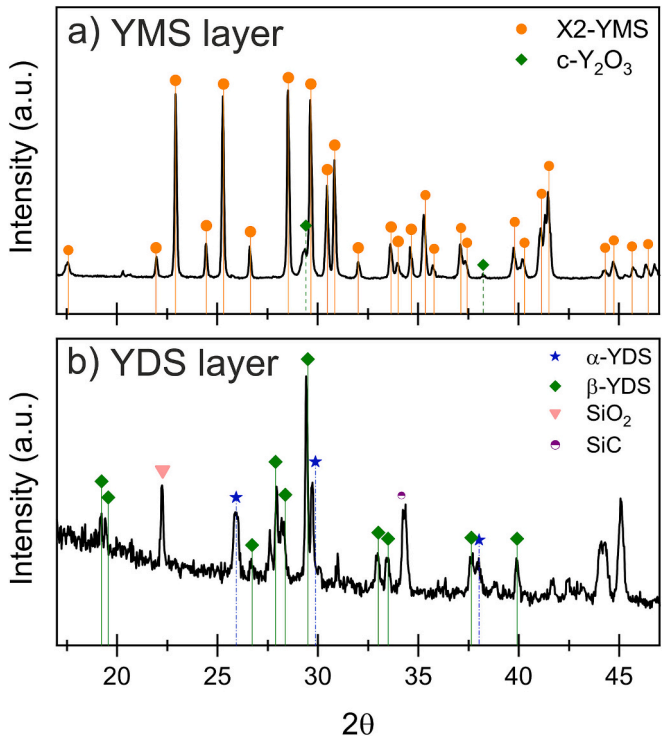

Fig. 3. XRD patterns of YMS and YDS layer after crystallization treatment for 2 h, at 1250 °C in air.

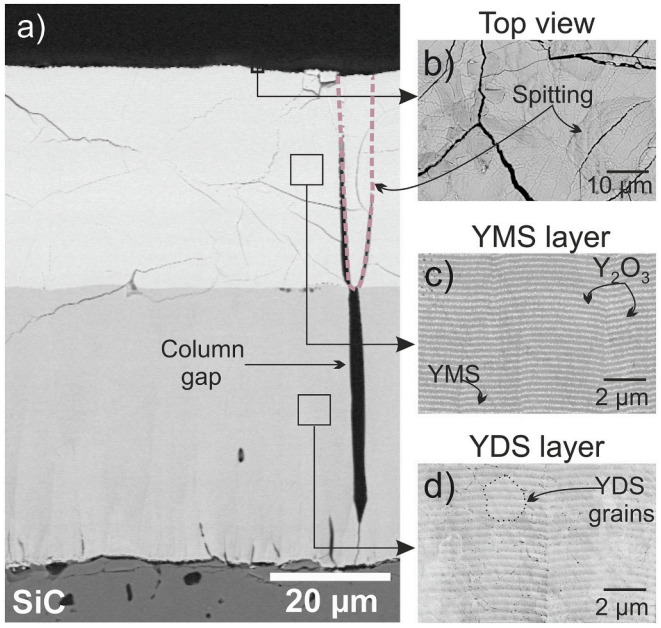

Fig. 4. Low- and high-magnification BSE micrographs of the EB-PVD YMS/YDS crystallized. (a) Overall cross-section of the layer, (b) surface (top view of YMS), (c) cross-section of YMS layer, and (d) cross-section YDS layer.

EBC microstructure after air isothermal oxidation for 100 h at 1400 °C. The grains on the YMS surface become better pronounced, and they are smaller after the oxidation test compared to the crystallized state (after crystallization: 5.6 ± 5.3 μm and after oxidation: 2.4 ± 1.9 μm, see Figs. 4b and 5a). Nonetheless, mud-type cracks seem to have further opened and spitting disorders are still present. The coating has undergone partial delamination after the oxidation. The cross-section (Fig. 5b) still reveals the dense columnar microstructure with few fine internal cracks, which are predominantly present in the top YMS layer. However, oxidation leads to the formation of dark inclusions in the crack-free YDS layer. XRD has confirmed that the YMS layer predominantly consists of X2-YMS with a small contribution from Y_2O_3 (Fig. 3a). The peak ~29.4° may be related to the YDS layer and is addressed afterwards. As expected, XRD analysis confirmed the presence of β-YDS and minor peaks around 22° related to silica (presumably formed at the EBC/SiC interface). A slight increase in the thickness of each layer was observed (compared to the crystallized coating), especially noticeable in YMS (+1.2 μm), whereas it is negligible in YDS (0.3 μm) as shown in Table 1.

Table 1
Thickness changes of the YMS and YDS layers after air and wet condition oxidation tests.

Layer	As-deposited (μm)	Crystallized (μm)	Air, 1400 °C (μm)	Wet, 1300 °C (μm)	Wet, 1400 °C (μm)
YMS	33.7	34.7	35.9	36.2	36.3
YDS	38.3	42.7	43	43.8	44.3

3.4. Isothermal oxidation under wet condition

Following 100 h of oxidation at both 1300 and 1400 °C the EBC coatings undergone a complete spallation. BSE micrographs of top view and cross-sections are presented in Fig. 5c to f. The top view of YMS at 1300 °C reveals that the surface is covered by ridges and surprisingly partially healed macroscopic cracks. On the other hand, at 1400 °C, the ridge size has considerably increased, and crack healing was more evident (Fig. 5e).

The cross-sectional morphology of the YDS layer exhibited dense elongated columns, separated by aligned pores in the direction of intercolumnar gaps (Fig. 5d,f) at both temperatures. At 1400 °C (Fig. 5b,f) the YDS layer reveals more significant regions with larger dark inclusions as clusters compared to at 1300 °C (Fig. 5d). The darker color (BSE contrast) of the small grains implicates that it contains the lighter element, but the grain size was too small for EDS analyzes in SEM. The reaction of the YMS layer with water vapor has increased the defect density (pores, microcracks), mainly at top of the column and at intercolumnar pores. In the YMS layer treated at the high temperature (1400 °C), the pore size increased and the layer contains additional white grains (Fig. 5f). The YMS/YDS interface is characterized by a series of pores, which are predominant at 1400 °C compared to 1300 °C (Fig. 5f).

The average thickness of YMS and YDS layers before and after oxidation tests were compiled in Table 1. As expected, the maximum change was observed under wet condition in combination with higher temperature (1400 °C). A maximum increase of 1.6 μm in thickness was observed in both YMS and YDS layer. Both YMS and YDS layers were further investigated under TEM and presented in Figs. 7 and 8 to identify the phase changes during the oxidation.

3.4.1. YMS phase transformation during the oxidation under air and wet condition

The different contrasts in YMS cross-sectional micrographs (Fig. 5b, d,f) might correspond to the local concentration changes of Y and Si. XRD patterns on the YMS layer show the presence of X2-YMS as the primary phase as well as a secondary Y_2O_3 (Fig. 6a) under all conditions. The XRD results suggest the presence of additional signals related to an un-identified crystalline phase especially, the peak at 27.6° (1400 °C, wet condition) (Fig. 6a). However, peaks at ~27.5, 27.8, and 29.4° (1300 °C, wet condition) can be assigned to YDS, and further TEM analysis was done to confirm it.

TEM analysis on the wet condition EBCs has identified similar phases at both 1300 °C and 1400 °C treatments. Therefore, only TEM results from 1300 °C samples are presented in this work. High magnification

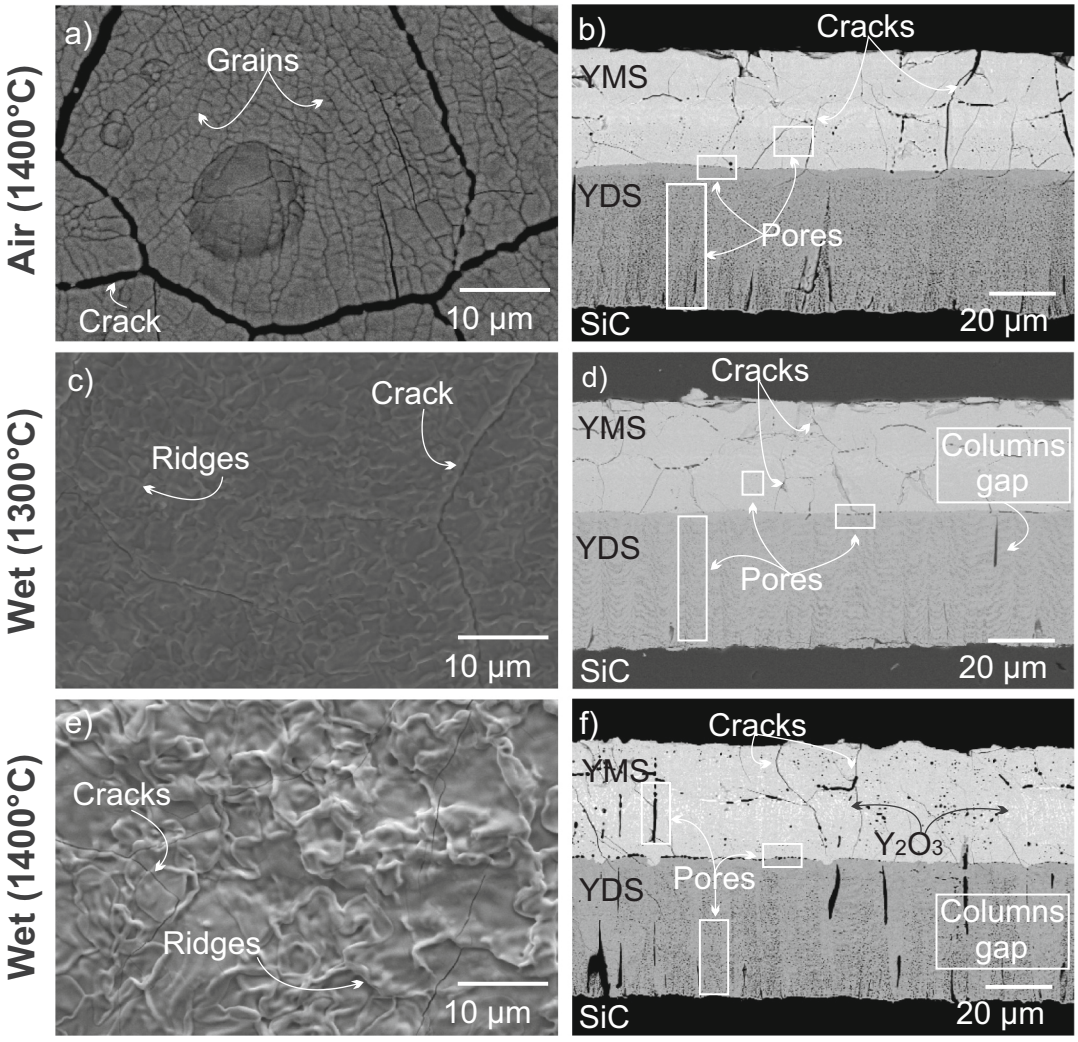

Fig. 5. BSE micrographs of EBC layers oxidized in air (100 h, 1400 °C, 100 % air) and water vapor at 1300 and 1400 °C (100 h, 30 %H_2O/70%wt air). The left column shows the top view (a, c, e), and the right column shows the cross-sections (b,d,f) of the respective layers.

micrograph of the YMS layer where a FIB lamella was prepared is presented in Fig. 7a. A HAADF STEM image shows the YMS lamella in which Zone I and II are marked (Fig. 7b). Zone I can be described as a homogeneous and dense matrix with an elemental ratio of 65Y—35Si, based on EDS analysis. The electron diffraction pattern obtained from zone I, unambiguously verified the X2-YMS phase by the zone axis patterns shown in Fig. 7c,d. The phase was indexed according to the monoclinic $Y_2Si_2O_5$ cell (ICSD 27003) with lattice parameters calculated as $a_0 = 14.6$ Å, $b_0 = 6.2$ Å, $c_0 = 10.5$ Å, and $\beta = 122.2°$. Zone II consists of mostly circular grains with the diameter of 10–100 nm (Fig. 7b,e). TEM-EDS analysis reveals a Y-rich composition on the grains, and the Fourier transform pattern confirms it as c-Y_2O_3 phase (Fig. 7f). In the case of 1400 °C, the Y_2O_3 particles coalesce to form larger grains of up to 3 μm, which are visible in the high magnification BSE micrograph (Fig. 7i).

Aleatory Al-rich crystals were found through the YMS lamella, namely the Zone III (Fig. 7g). Notice that in Fig. 7b, zone III is not immediately visible due to the lower contrast difference and magnification. Chemical analysis by TEM-EDS showed an average elemental concentration of 21.2 Al, 14.8 Si, and 85.3 Y, omitting the O content for zone III. TEM diffraction has confirmed those Al particles are assigned to an orthorhombic crystal structure with lattice parameters of $a_0 = 10.3$, Å $b_0 = 3.6$ Å, and $c = 10.5$ Å. Al-rich crystals were more predominant at 1400 °C (BSE micrograph Fig. 7j) compared to 1300 °C. The peak related to 27.6° in wet condition at 1400 °C may be related to the Al-phase. No evidence about the presence of YDS within the YMS layer was found in TEM analysis.

3.4.2. YDS phase transformation during the oxidation under air and wet condition

XRD powder patterns of the YDS layer after oxidation at both temperatures and conditions are given in Fig. 6b. The XRD measurement on silica that has grown on the SiC substrate at 1400 °C at the EBC/SiC interface is also presented in Fig. 6b for comparison. β-YDS phase was predominantly present in the coating at both temperatures (1300 and 1400 °C). However, at 1400 °C wet conditions, the peak at 29° might be associated to γ-YDS polymorph. The SiC surface has exhibited only peaks of SiO_2 and SiC. The weak peaks in YDS around 22° can be assigned to SiO_2 (part of SiO_2 from SiC surface was attached to YDS during the spallation).

A more detailed insight into the phase assemblage of the YDS layer was provided by analytical TEM and electron diffraction on FIB derived lamellae, as compiled in Fig. 8 for the “wet condition” specimen at 1300 °C for 100 h. A close-up of the YDS cross section showed the area where the lamella was prepared (Fig. 8a). A HAADF-STEM micrograph in Fig. 8b displays zone A consisting of small (~0.1 nm) and larger (>1 nm) dark inclusions, surrounded by an inclusion-free zone B.

EDS mapping of zones A and B reveals that these inclusions are SiO_2 pockets embedded in zone B as well as in channel pores (see Fig. 8c-e). A

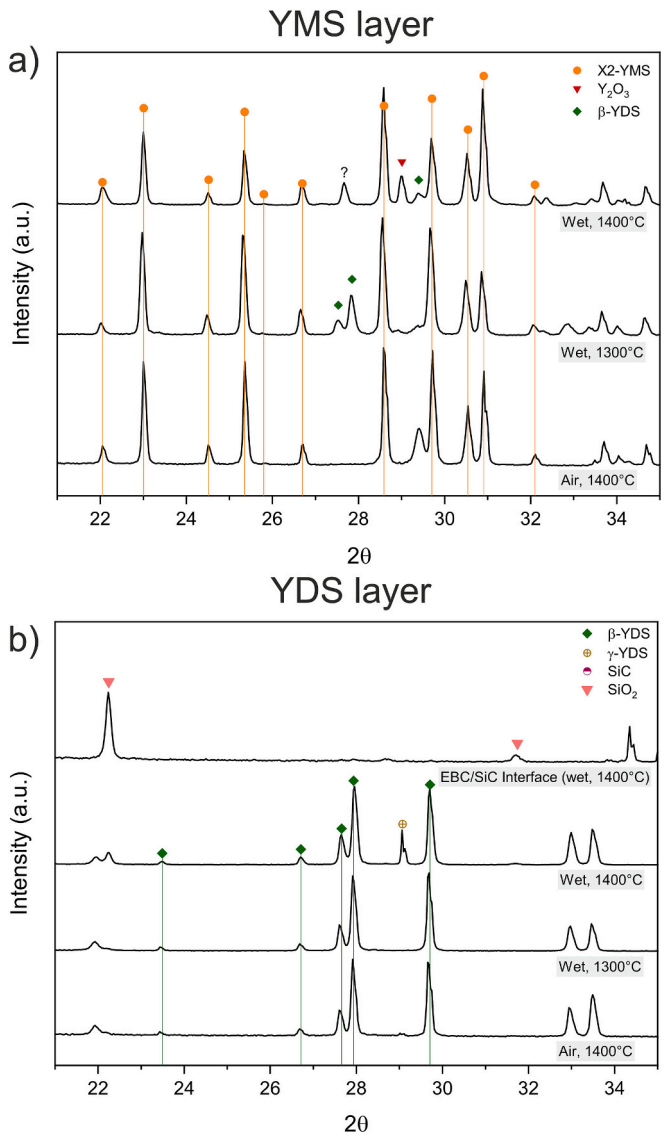

Fig. 6. XRD scans of the YMS (a) and YDS (b) layers after air and wet condition oxidation.

SAED pattern collected from one of the SiO_2 pockets, as well as tilt images (not shown) revealing the presence of an amorphous phase (Fig. 8f, g).

Zone B was analyzed using TEM-EDS confirming the YDS stoichiometry with a Y:Si ratio of 1:1. Likewise, the diffraction reveals that Zone B consists of the β-YDS polymorph (Fig. 8h,i). The zone axis pattern is depicted in Fig. 8i and was indexed according to the monoclinic $Y_2Si_2O_7$ cell as listed ICSD 281312. No evidence of the γ-YDS polymorph was found by TEM in the area accessible.

3.5. Oxidation of SiC substrate underneath the EBC system

Since a silica-forming Si-bond coat was missing and the current top layer EBCs do not fully prevent the oxygen inward diffusion, the underlying SiC has undergone oxidation under the studied conditions. Interesting observations were made on the oxidation of EBC-coated SiC substrate. Micrographs of the silica scale that has formed at the interface between SiC and EBC after 100 h of isothermal exposure is shown in Fig. 9. SiO_2 that has formed under air conditions (1400 °C, 100 h) with EBC on top are shown in Fig. 9a. Wet condition samples still show a few YDS grains on top of SiO_2 (white small particles after the EBC spallation) (Fig. 9b,c). The silica scale exhibits pores, which apparently got reduced in size as the temperature rose from 1300 °C to 1400 °C. The SiO_2 scale that has formed under air conditions has also experienced pore formation but thinner in comparison to the wet condition (Fig. 9a). Thickness measurements of the silica scale were determined via image analysis, and at least 15 data points were considered for each sample which are presented in the form of a box and whisker plots in Fig. 10. It is worth mentioning that some of the silica formed may have adhered to the YDS layer after spallation. The silica thickness measurements were only done on the SiC surface. In the plot, the box represents the first (bottom line) and third (top line) quartile of the thickness data. The upper and lower lines are the maximum and minimum values. At 1400 °C, air condition exposed specimens showed a median value significantly lower (4.7 μm) than in comparison with wet condition (5.7 μm). At 1300 °C, wet condition has resulted in the formation of a thick scale silica at the interface (6.6 μm, median value).

4. Discussion

4.1. Microstructure evolution

For the first time, a dual-layer EBC system consisting of thick YMS/YDS layers was successfully produced by the EB-PVD method. The optimization of the evaporation behavior of Y_2O_3 and SiO_2 was challenging and complicated but was achieved by adjusting the electron beam parameters such as beam jumping frequency, e-beam power, chamber pressure, etc. However, sometimes unstable silica melt pool has led to several spitting events that initiated local irregular overgrown and disordered parts in the coating (Fig. 1). It must be noted that silica as a glassy ingot is transparent which makes the optical observation of the melt pool and assessment of the evaporation conditions quite challenging. Further optimization of the evaporation conditions is necessary to avoid this spitting, and perhaps an optimization of the ingot microstructure may be also advisable. The applied process achieved relatively dense EBC, amid few cracks, with good adherence to the SiC substrate. Cracks might occur due to the internal stresses that arise during the cooling phase of the deposition procedure, and perhaps additional cracks may have formed during the metallographic preparation. The microstructural evolution of the EB-PVD EBC coating can be described on the basis of the well-known Movchan and Demchishin diagram, which is a function of the homologous temperature which is the quotient of substrate temperature (T_s) and melting point of the coating material (T_m). In this work, the evolved EBC microstructure could fall in zone 2, where dense columnar grains with smooth and faceted surfaces (Fig. 2) grow. Nevertheless, thin YMS/YDS columns (2-5 μm) grew perpendicularly to form a dense EBC coating. Due to the higher density of the coatings, feather arms and inter-columnar porosity as common in the case of TBCs was not observed. Columns typically exhibited a cauliflower microstructure at the surface, with narrow gaps between the columns. However, these gaps were not extended deep into the coating. In contrast, 7YSZ TBCs and zirconia-based materials which also fall in zone 2 [24], have been characterized by their particular pyramidal shape, feather arms, and columnar porosity. These results clearly point out the differences between the evaporation and condensation behavior of silica-based material (YMS or YDS) and zirconia-based materials.

On the other hand, the coatings' chemistry is governed by the ingot evaporation rate and the sample position, especially in the case of the jumping beam evaporation. Silica is challenging to evaporate as it sublimates compared to Y_2O_3, and the glassy nature makes observation of melting difficult. A stable cloud of Y_2O_3 was observed during the process. Meanwhile, an unstable cloud of silica was present. Due to the position variation of the samples for the first and second run, different stoichiometries were achieved. Y- rich composition (YMS) was obtained closer to the Y_2O_3 cloud, and an equal ratio for Si and Y (YDS) was achieved at an intermediate position between the two clouds.

Moreover, the jumping frequency is another critical parameter when

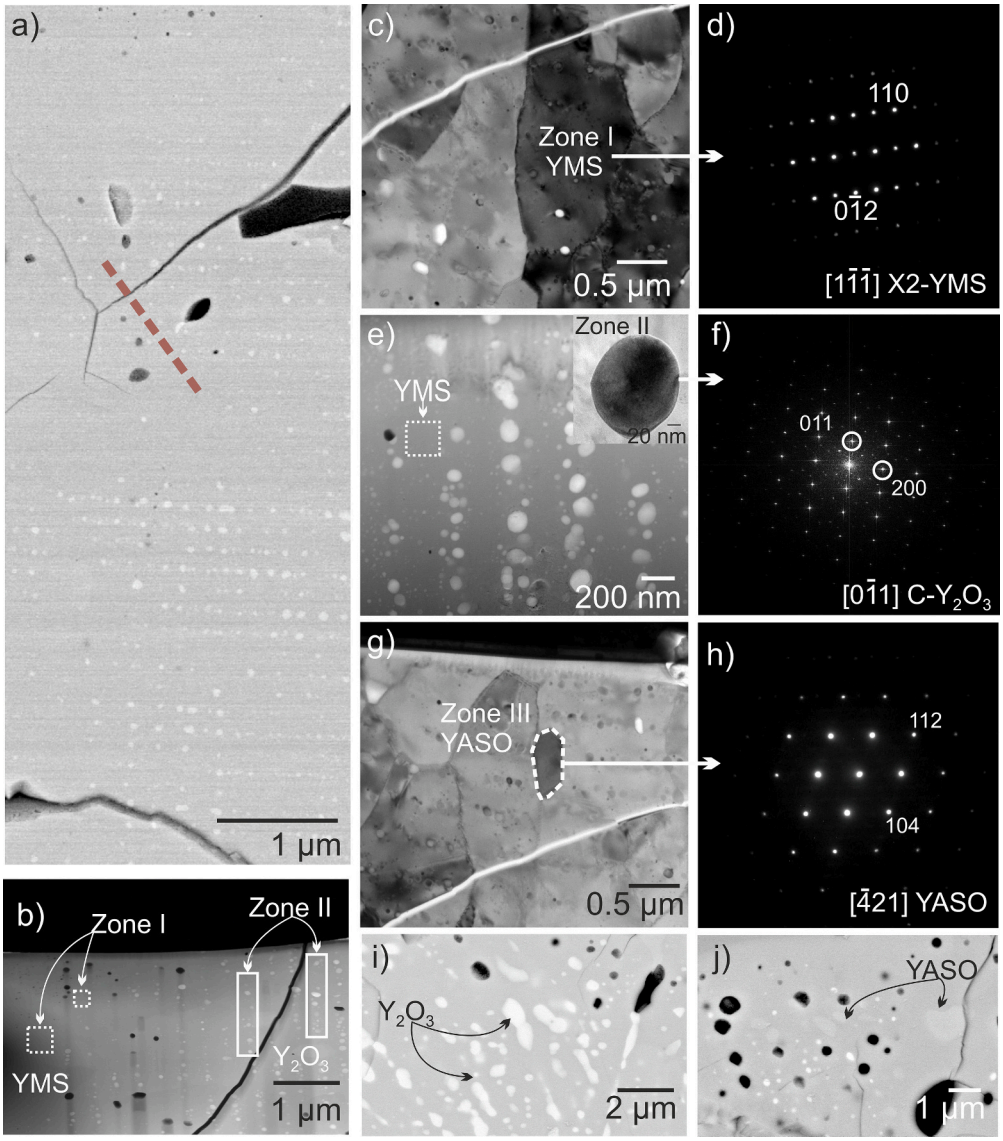

Fig. 7. (a) SEM micrograph showing the location of the TEM lamella taken from the YMS layer after oxidation at 1300 °C wet condition. (b) HAADF-TEM view of the lamella showing the zones I and II. Selected area electron diffraction (SAED) for zone I (c) and zone III (f) associated with X2-YMS and Al-phase. (e) Dark field STEM micrograph of zone II, Y_2O_3 particles. The zone axis pattern was obtained from YMS (d), Y_2O_3 (f), and Al-phase (h). BSE micrographs for the sample at 1400 °C show the coalescence of Y_2O_3 grains (i) and larger grains of Al-phase near the top column (j).

two sources are heated by a single electron beam. This critical frequency can be established according to the solidification time required for a material once the electron beam is withdrawn from the molten pool. For the final microstructure, a multilayer may form below the critical frequency. In addition, the rotation of the sample results in the formation of a nano-layered microstructure (Fig. 2d,e). Since the trial runs prior to the deposition of the investigated coatings were only limited in number, the perfect position and stable evaporation conditions from two pools for getting stochiometric YDS and YMS was not yet well established, which caused the deviation in chemistry from the ideal YDS and YMS ion ration.

4.2. Crystallization process of EB-PVD EBC multi-layer

It has been shown that the EBCs that are manufactured by either APS or reactive magnetron sputtering, require a crystallization heat treatment after deposition to achieve the desirable phases [8–11]. Similarly, the EB-PVD EBCs produced in this work were also found to be amorphous in the as-deposited condition. The applied crystallization heat-treatment in this study has increased both the presence of cracks (Fig. 4a,b) and the coating thickness by 3 and 10 % for YMS and YDS layers (Table 1), respectively. The rise in thickness can be attributed to the formation of Y_2O_3 and YMS phases during the transition of amorphous YMS composition into the crystalline state. In addition, the difference between the CTEs of Y_2O_3 (9.5×10^{-6}/K) and YMS (7.7×10^{-6}/K) [25] and the SiC substrate (4.5×10^{-6} /°K) could lead the crack formation during quenching. Similar phenomenon could have caused the thickness change and the crack formation in the case of YDS, where both α (CTE of 8×10^{-6}/K) and β (4.1×10^{-6}/K) YDS polymorphs evolved during crystallization.

After heat-treatment, no drastic change in the overall morphology of the coatings was observed. Thin intercolumnar gaps were present at few places. Larger columnar gaps due to spitting behavior were also observed randomly. Most importantly, a sharp interface between top YMS and bottom YDS layers was established after the heat-treatment. Homogenized YDS microstructure was achieved after heat-treatment. In the case of YMS layer, alternative nano-layers of Y_2O_3 and YMS were formed as an effect of their individual chemistry e.g., Y- or Si-rich

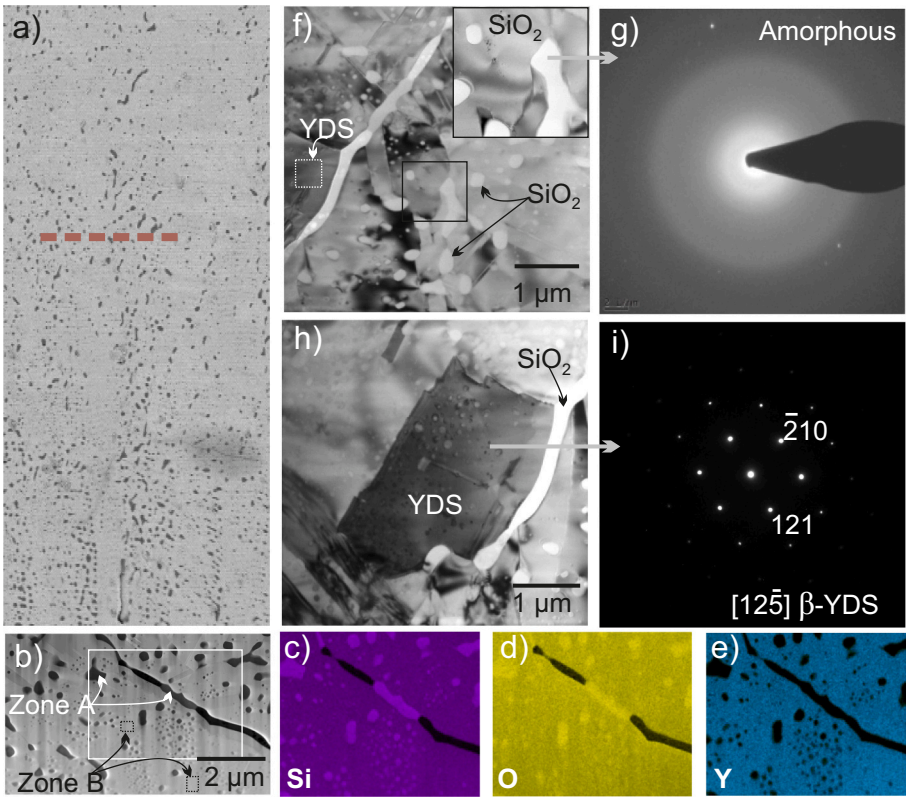

Fig. 8. (a) Cross-sectional SEM micrograph of the YDS layer showing the location of TEM lamella after oxidation under wet condition at 1400 °C. (b) HAADF-TEM view of the porous (zone A) and dense zone (zone B). (d-f) Associated Si, O, and Y, respectively, elemental maps. (g-h) SAED focused on SiO_2 pockets (zone A) and their corresponding patterns. (i-j) Dark field STEM micrograph emphasized zone B (YDS), and their zone axis patterns confirmed β-YDS.

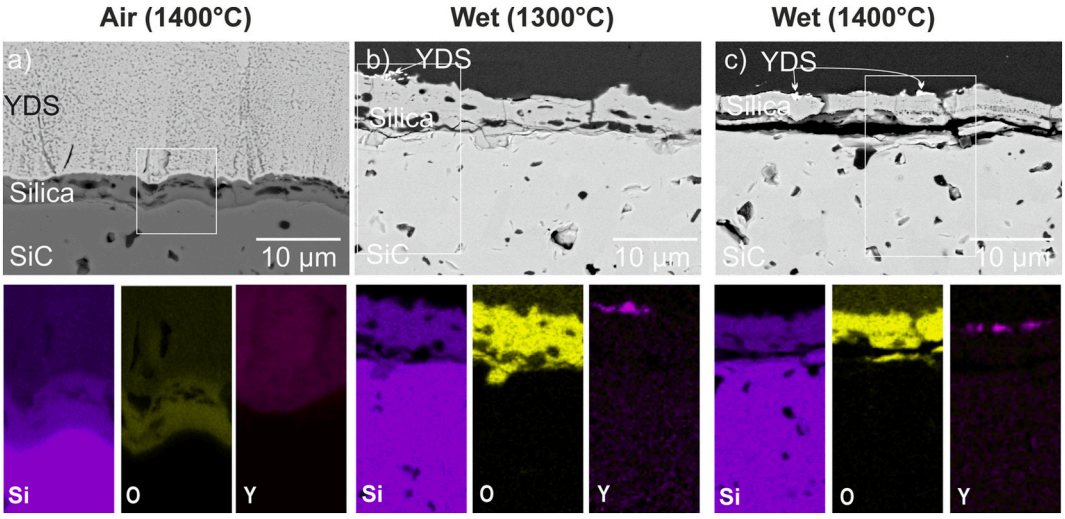

Fig. 9. BSE cross-sectional micrographs and chemical mapping of silica scale formed on top of SiC underneath YDS/YMS after 100 h, (a) under air at 1400 °C, (b) under wet condition at 1300 °C and (c) under wet condition at 1400 °C.

layers (Fig. 4c). The nano-layer formation is typically observed in the EB-PVD deposition process as a result of substrate rotation. In the case of TBCs, layered periodicity in the coating can reduce the phonon scattering and transport, leading to lower thermal conductivity [26]. Thus, layered periodicity will be engaging in improving the thermal conductivity of disilicate materials for EBCs. On the other hand, the desired single-phase composition for each layer is not achievable if the nano-layer thicknesses are too large. This can be compensated by a larger rotational speed which leads to a smaller thickness of each nano-layer.

4.3. EBC oxidation

EB-PVD EBCs are still in the early stages of development, and their performance under dry or wet oxidation conditions, thermal cyclic behavior, CMAS (calcio-magnesio-alimunio-silicate) resistance etc., must be studied in detail. This work seeks to provide the first results regarding water vapor oxidation. Generally, EBC steam oxidation has been studied in the laboratory using isothermal heat treatments, thermo cycle tests, and high temperature and velocity steam rigs where the

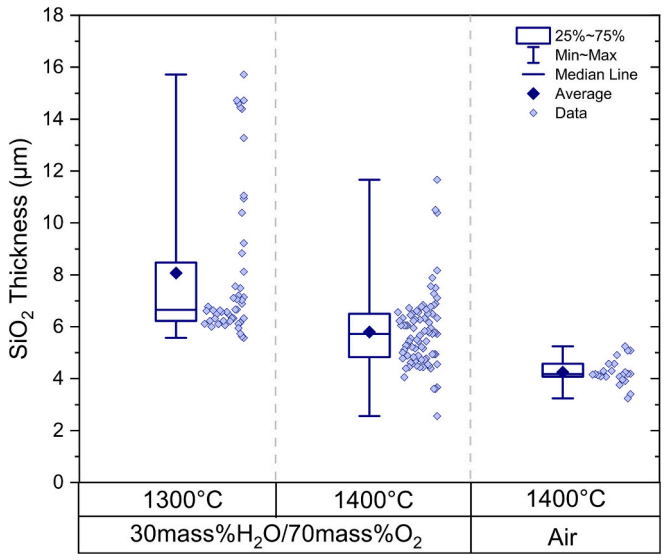

Fig. 10. Box and whisker plot of silica scale thickness measurements via image analysis after exposure in air and wet condition at 1300 and 1400 °C.

engine-like conditions were simulated, e.g., 30 atm total, 3 atm water vapor partial pressure, 100 m/s gas velocity, 1400 °C gas temperature in the combustor [8]. However, those aggressive tests could provide information about the radical degradation of EBCs under real engine conditions, but merely reveal the fundamental mechanisms of EBC degradation. Hence, a more careful approach of employing low water vapor flow rates at isothermal conditions was chosen in this study an initial step.

4.3.1. Degradation of EBC under air and wet oxidation

The topography of the EBC surfaces evidently showcases the differences between air and wet condition oxidation (Fig. 5). In air condition, the grain size reduction can be related to the sintering effect at 1400 °C after 100 h. The sintering causes the shrinkage of the surfaces, leading to larger cracks. Reduced size of the cracks with increased ridge sizes were observed on the surface after wet condition oxidation test (see Fig. 5c,e). The presence of ridges has been reported as an effect of SiO_2 volatilization from the grain boundaries of the bulk ceramic [27]. In this work, the ridge microstructure becomes more evident at 1400 °C compared to 1300 °C. This explicitly shows the temperature effect for the same low water vapor flow rates. Under a wet environment, this silica volatilization could be enhanced and lead to faster SiO_2 depletion at the surface, creating ridged structures and initiation of smaller cracks [10,27].

The exposure of YMS/YDS to air and wet condition has resulted in the opening up of intercolumnar porosity and the formation of closed pores in YMS and dark inclusions in YDS. The presence of closed pores has increased with increasing temperature (more at 1400 °C compared to 1300 °C, Fig. 5b,d,f). The pores could have formed due to SiO_2 loss during the formation of $Si(OH)_{4(g)}$ from YMS, or due to the coalescence of nano-pores. The nano-layers of Y_2O_3 and YMS have disappeared in the YMS layer after both oxidation conditions. Larger Y_2O_3 grains appear presumably due to the difference in internal energy, sintering and chemical potential form the yttria-rich nano-layers (see larger white grains in Fig. 7i). It must be noted that flow rates are not aggressive enough to cause substantial recession of the YMS, but they are just enough to cause silica loss and closed pore formation. Higher intra-columnar pores in YDS could be an effect of its lower sintering temperature (YMS ~1500 °C and YDS ~1402 °C) [28]. It is known from the literature that the formation of secondary phases during the silica volatilization leads to volume changes and causes a considerable thickness variation. However, the current study's thickness change was negligible (~1 µm as shown in Table 1). In addition to the morphological changes in the EBC layers, associated phase changes in both YDS and YMS layers were identified and are summarized in Table 2. It is known that yttria offers good resistance against water vapor. The SiO_2 activity for $Y_2SiO_5 + Y_2O_3$, is in the range of 0.002 which is lower than $Y_2SiO_5 + Y_2Si_2O_7 = 0.4$ [28]. Therefore, presence of little Y_2O_3 in YMS layer should offer better water vapor protection provided no additional CTE related issues are provoked.

The Al-phase (elemental concentration of 21.2 Al, 14.8 Si, and 85.3 Y) would have been most likely formed due to the reaction of the YMS layer with $(Al(OH)_{3\ (g)})$ resulting from the alumina tube reaction with water vapor while subjected to high temperature for longer times (1300 °C and 1400 °C, 100 h) (Fig. 7j) [29]. YAP ($YAlO_3$) and YAM ($Y_4Al_2O_9$) are two of the four crystalline phases occurring in the Al_2O_3-Y_2O_3 system with orthorhombic and monoclinic structures, respectively [30]. The Al-phase observed in this study exhibits similar stoichiometry to YAM, however, the crystal structure determined by TEM corresponds to an orthorhombic system (Fig. 7g). Matusch has investigated the Y_2O_3-SiO_2-Al_2O_3 system and reported the YASO phase as a partial solid solution with formula $Y_4Al_{2-2x}Si_{2x}O_{9+x}$ with a solubility range of $0.076 < x < 0.144$. The Al-phase identified in this study exhibits similar composition and crystal structure. Additional studies are required to identify and demonstrate the presence of YASO phase as this phase could be an interesting candidate for EBC material for oxide-oxide CMCs.

No evidence of YDS presence in YMS layer was found by TEM in contrary to the XRD (Fig. 7) reflections at ~27.5, 27.8 and 29.4° (Fig. 6a). It might be possible that X-rays were passing through the cracks in YMS layer and reach the underlying YDS layer. However, more experiments are needed to confirm this phenomenon.

The degradation mechanism of YDS under steam oxidation is documented well in the literature. SiO_2 volatilization causes the formation of a porous YMS phase, which further degrades to Y_2O_3 under continuous water vapor flow at high velocities (>150 m/s) [28,31]. XRD and TEM results of the YDS layer did not show evidence of either YMS or yttria (Figs. 6b and 8). Nevertheless, numerous silica inclusions (amorphous) have been identified within the YDS layer (Fig. 8b-e). The YDS coating has excess silica in its as coated state (Y:Si = 0.75) and it is believed that the observed SiO_2 pockets are formed as a result of segregation during the high temperature exposure. It can be concluded that the EB-PVD YMS top layer has fully protected the underlying YDS layer against water vapor reaction. However, the γ-YDS polymorph was observed after oxidation, see Fig. 6. The evaluated temperature range between 1300 °C and 1400 °C represents the widely accepted YDS polymorphic transformation temperature according to the disilicate phase diagram [32]. The temperature range of β → γ transition lies between 1320 and 1445 °C [32]. The temperature tested and the cooling conditions may be associated with the formation of YDS polymorphous.

After the crystallization heat treatment, EBC showed cracks, mainly in the YMS layer (Fig. 3). Cracks work like channels that favor oxygen and water vapor transport and promote porosity. Assuming the water vapor diffused through pores and cracks along the YMS crack, the YDS layer should have undergone the aforementioned degradation. However, this was not observed (Fig. 5) under the experimental conditions used in this study. Consequently, the cracks in YMS did not trigger steam

Table 2
Summary of resulted phases after air and wet condition in YMS and YDS layer.

Oxidation test	Temperature (°C)	Phases resulted on YMS Layer	Phases resulted on YDS Layer
Dry air	1400	YMS Y_2O_3	β-YDS SiO_2 -amorphous
Water vapor	1300	YMS Y_2O_3 Al-phase	β-YDS SiO_2 -amorphous
Water vapor	1400	YMS Y_2O_3 Al-phase	β-YDS γ-YDS SiO_2 -amorphous

reactions in YDS.

4.4. SiC oxidation behavior

The impact of the dual-layer EB-PVD EBC without a Si bond coat on the silica scale formation was assessed under air and wet conditions. As expected, SiC has been oxidized, and a silica scale has formed underneath the EBC layers.

All silica scales exhibited channel cracks, which can be attributed to the β → α-SiO_2 (cristobalite- > quartz) transformation, as shown in Fig. 9 [4,8,9]. In addition, growth stresses can also contribute to the formation of cracks (Fig. 9 a,b,c). After wet condition, the spallation of the EBC may have also enhanced the cracks in the silica scale. Oxide scale thickness measurements prove that water vapor has enhanced the SiO_2 scale growth. Surprisingly, this effect is more pronounced at 1300 °C than at 1400 °C, but the EBC spallation may have biased the accuracy of some data.

The scale was found to be more porous and perhaps thicker at 1300 °C, compared to 1400 °C (Figs. 9b and 10). The presence of bubbles (pores) in the SiO_2 scale resulted from the formation of gaseous species such as CO and its rapid outward diffusion during the oxidation of SiC [33]. On the other hand, it is known that silica, which is grown at lower temperatures (1200 °C), is mainly amorphous and increases its crystallinity as the temperature increases (1300 °C and 1400 °C) [34]. Thus, silica formed at 1400 °C may be more crystalline than silica formed at 1300 °C. Opila proposed that the gaseous products (CO) are more soluble in crystalline SiO_2 at high temperatures. Moreover, there is a different interaction between the hydroxyl group and the SiO_2 polymorphs (crystalline or amorphous). Considering these findings, at 1300 °C, more CO would have been trapped in silica during the oxidation of SiC inducing more significant porosity and higher thickness (Fig. 10). At 1400 °C, lack of bubbles might have led to the contraction of the silica scale (hence thinner), which was observed in Fig. 10 [4,8,9].

At 1400 °C, the difference in the silica scale thickness between wet and air conditions is only 1 μm. This suggests that the applied EBCs have offered protection to the underlying SiC substrate. It is expected that this effect would have been more evident in the presence of a Si-bond coat. The most significant observation in the case of wet condition is the spallation of EBC layers, which could be the result of a non-uniform thickness and wavy silica scale formation compared to a slightly thinner and uniform scale under air condition (see scattering in the thickness measurements as shown in Fig. 10). This is agreement with the literature that the growth stresses are responsible for the spallation of thick SiO_2 scales, which have crossed critical thickness values of ~4–5 μm [35]. A proper Si-bond coat might have reduced the silica growth and provided better adherence to the EBC layers.

4.5. Challenges for EB-PVD focused in EBC application

This work has demonstrated the feasibility of EB-PVD to produce EBC layers. Moreover, the versatility of developing new microstructures like dense or columnar EBCs has been proven again. In comparison to sputtered PVD EBCs, the high evaporation and condensation rates would allow the production of thicker coatings on sharp edges and curved geometries. In addition, using multiple ingots opens up the possibility of producing multi-component T/EBC, providing the evaporation parameters are optimized. Based on the developed EB-PVD TBC know-how, the EBC microstructure can be modified in order to enhance the critical properties such as thermal conductivity (by multiple nano-layers), high strain tolerance, and erosion resistance. Efforts are ongoing to modify the EBC microstructure by adding a Si-bond coat and optimizing the evaporation conditions. In this context, a huge scope exists for the optimization of EB-PVD produced EBCs and leads the way for the development of complex EBCs or T/EBCs with even more promising microstructural features and performance.

5. Conclusions

A multi-layer EBC system was produced on top of a SiC substrate by co-evaporation of two ingots (SiO_2 and Y_2O_3), using the EB-PVD methodology for the first time. YMS and YDS layers were successfully deposited as amorphous layers close to the nominal stoichiometric composition, but still with a not neglectable deviation. A mostly dense columnar coating without larger inter-columnar gaps or feather arms of around ~40 μm thickness for each layer was achieved. X2-YMS and yttria were crystallized as major phases constituents of the YMS while the YDS layer consisted mainly of α- and β-YDS after the crystallization treatment at 1250 °C. The crystallization of the amorphous coating has led to an increase in coating thickness and the evolution and progression of some cracks in the EBC.

High temperature oxidation under air and water vapor conditions was performed to investigate the thermochemical stability and microstructural evolution of YMS/YDS EB-PVD EBC. Under wet conditions, SiO_2 volatilizes, forming ridges on the YMS surface, and crack healing was observed. A rise in temperature from 1300 °C to 1400 °C has enhanced the SiO_2 evaporation rate and formation of yttria and pores within the YMS layer. No evidence of YDS destabilization into YMS was observed. Under both air and wet oxidation conditions (100 h, 1300 and 1400 °C), the β-YDS polymorph was found to be stable and the mixture of X2-YMS and yttria remained in the YMS layer while in the YDS layer the α-polymorph has disappeared.

A silicon bond coat is required for attaining better adherence between SiC and the EB-PVD EBCs. Oxidation of SiC has led to the formation of a non-uniform, porous silica layer at the interface, which was found to be thicker under wet than under air conditions. Under the studied conditions, EB-PVD EBCs have proven to be effective against SiC water vapor enhanced oxidation.

CRediT authorship contribution statement

Cynthia Y. Guijosa-Garcia: Writing – original draft, Methodology, Investigation, Formal analysis, Data curation, Conceptualization. **Klemens Kelm:** Writing – review & editing, Methodology, Investigation. **Uwe Schulz:** Writing – review & editing, Validation, Conceptualization. **Ravisankar Naraparaju:** Writing – review & editing, Visualization, Validation, Supervision, Conceptualization.

Declaration of competing interest

The authors declare the following financial interests/personal relationships which may be considered as potential competing interests: Cynthia Yanel Guijosa Garcia reports financial support was provided by German Academic Exchange Service - DAAD. If there are other authors, they declare that they have no known competing financial interests or personal relationships that could have appeared to influence the work reported in this paper.

Acknowledgments

The authors acknowledge the support of the German Academic Exchange Service (DAAD). For the technical support at the German Aerospace Center, the authors thank D. Peters, J. E. Förster and F. Kreps. Additionally, the authors would like to thank P. Mechnich for the scientific discussions.

Data availability

The data that has been used is confidential.

References

[1] J. Steibel, Ceramic matrix composites taking flight at GE Aviation, Am. Ceram. Soc. Bull. 98 (2019) 30–33.

[2] K.N. Lee, in: J.L. Narottam P. Bansal (Ed.), Ceramic Matrix Composites: Materials, Modeling and Technology 2014, 2014, pp. 430–451.

[3] D.M. Nathan Jacobson, Elizabeth Opila, Evan Copland, *Journal of Physics and Chemistry of Solids*, Interactions of water vapor with oxides at elevated temperatures 66, 471–478 (2005). doi:https://doi.org/10.1016/j.jpcs.2004.06.044.

[4] E.J. Opila, Oxidation and volatilization of silica formers in water vapor, J. Am. Ceram. Soc. 86 (2003) 1238–1248, https://doi.org/10.1111/j.1151-2916.2003.tb03459.x.

[5] K.N. Lee, Protective coatings for gas turbines, in: The Gas Turbine Handbook 4.2, 2006.

[6] N.P. Padture, Environmental degradation of high-temperature protective coatings for ceramic-matrix composites in gas-turbine engines, npj Mater Degrad 3 (2019), https://doi.org/10.1038/s41529-019-0075-4.

[7] N.P. Padture, Advanced structural ceramics in aerospace propulsion, Nat. Mater. 15 (2016) 804–880, https://doi.org/10.1038/nmat4687.

[8] R.V. Emine Bakan, Oxidation kinetics of atmospheric plasma sprayed environmental barrier coatings, J. Eur. Ceram. Soc. 42 (2022) 5122–5128, https://doi.org/10.1016/j.jeurceramsoc.2022.05.003.

[9] K.A. Kane, E. Garcia, S. Uwanyuze, M. Lance, K.A. Unocic, S. Sampath, B.A. Pint, Steam oxidation of ytterbium disilicate environmental barrier coatings with and without a silicon bond coat, J. Am. Ceram. Soc. 104 (2021), https://doi.org/10.1111/jace.17650.

[10] Vito Leisner, Klemens Kelm, Uwe Schulz, Thin single-phase yttrium-based environmental barrier coating systems for SiC/SiC CMCs, J. Eur. Ceram. Soc. 42 (2022) 7275–7287, https://doi.org/10.1016/j.jeurceramsoc.2022.08.035.

[11] R. Anton, V. Leisner, N. Laska, U. Schulz, Reactive sputtered ytterbium silicate environmental barrier coatings for protection of Mo-Si-based alloys, Coatings 12 (2022) 1086, https://doi.org/10.3390/coatings12081086.

[12] W.A. Kaysser, M. Peters, K. Fritscher, U. Schulz, Processing, characterisation and testing of EB-PVD thermal barrier coatings, in: AGARD SMP Meeting on Thermal Barrier Coatings, 1997.

[13] M.H.R. Naraparaju, U. Schulz, P. Mechnich, Tailoring the EB-PVD columnar microstructure to mitigate the infiltration of CMAS in 7YSZ thermal barrier coatings, J. Eur. Ceram. Soc. 37 (2017) 261–270, https://doi.org/10.1016/j.jeurceramsoc.2016.07.027.

[14] L.C.S. Mikulla, P. Niemeyer, U. Schulz, R. Naraparaju, Microstructure refinement of EB-PVD gadolinium zirconate thermal barrier coatings to improve their CMAS resistance, Coatings 13 (2023) 195, https://doi.org/10.3390/coatings13050905.

[15] R.P.P.R. Naraparaju, P. Mechnich, U. Schulz, EB-PVD alumina (Al2O3) as a top coat on 7YSZ TBCs against CMAS/VA infiltration: Deposition and reaction mechanisms, J. Eur. Ceram. Soc. 38 (2018) 3333–3346, https://doi.org/10.1016/j.jeurceramsoc.2018.03.027.

[16] J.J.G.C.R. Naraparaju, U. Schulz, C.V. Ramana, Interaction and infiltration behavior of Eyjafjallajökull, Sakurajima volcanic ashes and a synthetic CMAS containing FeO with/in EB-PVD ZrO2–65 wt% Y O3 coating at high temperature, Acta Mater. 136 (2017) 164–180, https://doi.org/10.1016/j.actamat.2017.06.055.

[17] R.N. Juan, J. Gomez Chavez, Peter Mechnich, Klemens Kelm, Uwe Schulz, C. V. Ramana, Effects of yttria content on the CMAS infiltration resistance of yttria stabilized thermal barrier coatings system, J. Mater. Sci. Technol. 43 (2020) 74–83, https://doi.org/10.1016/j.jmst.2019.09.039.

[18] J.B.H. Dongming Zhu, Advance High Temperature Environmental Barrier Coating System for SiC/SiC Ceramic Matrix Composites US 10,807,912 B1, 2017.

[19] N.Y. Taishi Yokoi, Makoto Tanaka, Daisaku Yokoe, Takeharu Kato, Satoshi Kitaoka, Masasuke Takata, Preparation of a dense ytterbium disilicate layer via dual electron beam physical vapor deposition at high temperature, Mater. Lett. 193 (2017) 176–178, https://doi.org/10.1016/j.matlet.2017.01.085.

[20] A.L. Peter Mechnich, Reinhold Braun, Claudia Büttner, Y2SiO5 coatings fabricated by RF magnetron sputtering, Surf. Coat. Technol. 237 (2013) 88–94, https://doi.org/10.1016/j.surfcoat.2013.08.015.

[21] M.H. Lu, H.M. Xiang, Z.H. Feng, X.Y. Wang, Y.C. Zhou, J. Smialek, Mechanical and thermal properties of Yb2SiO5: a promising material for T/EBCs applications, J. Am. Ceram. Soc. 99 (2016) 1404–1411, https://doi.org/10.1111/jace.14085.

[22] L.R. Turcer, A. Sengupta, N.P. Padture, Low thermal conductivity in high-entropy rare-earth pyrosilicate solid-solutions for thermal environmental barrier coatings, Scr. Mater. 191 (2021) 40–45, https://doi.org/10.1016/j.scriptamat.2020.09.008.

[23] A.J. Fernández-Carrión, M. Allix, A.I. Becerro, M. White, thermal expansion of rare-earth pyrosilicates, J. Am. Ceram. Soc. 96 (2013) 2298–2305, https://doi.org/10.1111/jace.12388.

[24] H.-J.R.-S.U. Schulz Dr.-Ing., B. Saruhan, A.F. Renteria, Thermal conductivity issues of EB-PVD thermal barrier coatings, Mat.-wiss. u. Werkstofftech. 38 (2007) 659–666, https://doi.org/10.1002/mawe.200700189.

[25] V. Leisner, (Karlsruher Instituts für Technologie (KIT): 2019).

[26] J. Singh, D. Wolfe, Review nano and macro-structured component fabrication by electron beam-physical vapor deposition (EB-PVD), J. Mater. Sci. 40 (2005) 1–26, https://doi.org/10.1007/s10853-005-5682-5.

[27] N.P.N. Al Nasiri, D.D. Jayaseelan, W.E. Lee, Water vapour corrosion of rare earth monosilicates for environmental barrier coating application, Ceram. Int. 43 (2017) 7393–7400, https://doi.org/10.1016/j.ceramint.2017.02.123.

[28] E.J.O. Cory, G. Parker, Stability of the Y2O3–SiO2 system in high-temperature, high-velocity water vapor, J. Am. Ceram. Soc. 103 (2020) 2715–2726, https://doi.org/10.1111/jace.16915.

[29] D.L.M. Elizabeth, J. Opila, Alumina volatility in water vapor at elevated temperatures, J. Am. Ceram. Soc. 87 (2004) 1701–1705, https://doi.org/10.1111/j.1551-2916.2004.01701.x.

[30] R.H.M. Medraj, M.A. Parvez, R.A.L. Drew, W.T. Thompson, *Journal of the European Ceramic Society*, High temperature neutron diffraction study of the Al2O3–Y2O3 system 26, 3515-3524, 2006, https://doi.org/10.1016/j.jeurceramsoc.2005.12.008.

[31] K.M. Robert, A. Golden, Elizabeth J. Opila, *Journal of the American Ceramic Society*, Thermochemical stability of Y2Si2O7 in high-temperature water vapor. 103 (2020) 4517–4535, https://doi.org/10.1111/jace.17114.

[32] J. Felsche, Polymorphism and crystal data of the rare-earth disilicate of type RE2Si2O7 2I, J. Less-Common Metals 21 (1970) 1–14.

[33] B.H. Benjamin Kowalski, Thermally grown oxide in water vapor on coated and uncoated SiC, J. Am. Ceram. Soc. 103 (2020) 5978–5989, https://doi.org/10.1111/jace.17295.

[34] E.J. Opila, Variation of the oxidation rate of silicon carbide with water-vapor pressure, J. Am. Ceram. Soc. 82 (1999) 625–636, https://doi.org/10.1111/j.1151-2916.1999.tb01810.x.

[35] K.N. Lee, Yb2Si2O7 Environmental barrier coatings with reduced bond coat oxidation rates via chemical modifications for long life, J. Am. Ceram. Soc. 102 (2019) 1507–1521, https://doi.org/10.1111/jace.15978.